Characterization of the Al-Ga solid-liquid interface using classical and *ab initio* molecular dynamics simulation

Jesse L. Kern,[1] Peter R. Barry,[2] and Brian B. Laird[2,*]
[1]*Department of Chemistry, Randolph College, Lynchburg, Virginia 24503, USA*
[2]*Department of Chemistry, University of Kansas, Lawrence, Kansas 66045, USA*

(Received 19 July 2019; revised manuscript received 6 February 2020; accepted 16 March 2020; published 24 April 2020)

We present a detailed characterization of the structure and transport properties of aluminum–gallium solid–liquid interfaces using classical molecular-dynamics simulation and an embedded-atom model. In addition, *ab initio* molecular-dynamics simulations are performed to confirm the structural results from the classical force field. For the (100), (110), and (111) Al crystal orientations, we calculate density, potential energy, stress, and diffusion constant profiles as well as a two–dimensional Fourier analysis of the interfacial layers. We find that, for each crystal orientation, the first one to two layers of the Ga liquid have a lateral structure that is commensurate with the underlying Al substrate. *Ab initio* molecular-dynamics simulations of a smaller system size for the (100) and (111) orientations were also performed. The results support the liquid absorption behaviors from the larger scale classical simulations.

DOI: 10.1103/PhysRevMaterials.4.043604

I. INTRODUCTION

The determination of the structural, thermodynamic, and transport properties of chemically heterogeneous solid–liquid interfaces (SLIs) is important for understanding a number of technologically relevant processes such as wetting and nucleation [1]. In particular, chemically heterogeneous metal-metal SLIs are especially difficult to study experimentally because both phases are opaque to standard spectroscopic probes. As a consequence, much of our understanding of such interfaces comes from atomistic simulation.

Previous simulation studies on chemically heterogeneous metal–metal SLIs include those on aluminum–copper [2], copper–lead [3,4], aluminum–lead [5,6], and tantalum-copper [7]. Geysermans *et al.* examined the interface between solid Cu and liquid Al at 1000 K and found that the Cu crystal induces significant liquid Al density layering at the interface with the first layer of liquid Al showing a lateral ordering commensurate with the copper (100) and (111) surfaces, although with significant vacancies, due to the substantial mismatch between Cu and Al. In a study of the Cu(s)/Pb(l) SLI at 625 K, Palafox-Hernandez *et al.* observed that significant surface alloying occurs on the (100) interface. Additionally, they observed Pb prefreezing on the (111) Cu surface in which two to three layers of crystalline Pb form at the Al surface. These Pb crystal layers are compressed by about 2% versus the expected bulk lattice constant and rotated by about 6° relative to the surface Cu layers. This prefreezing layer was found to yield a significantly larger heterogeneous nucleation rate upon undercooling relative to the (100) interface [4]. Y. Yang *et al.* [5] examined the interface between solid Al and liquid Pb at 625K and found considerable anisotropy in the structural and transport properties for the (100), (110), and (111) interfaces. At this temperature, the (111) interface is faceted, but the (100) and (110) interfaces are rough, with minor interlayer peaks in the density profile located between the first interfacial solid and liquid peaks. It was also observed that this system has an interfacial premelting transition at higher temperatures [6]. In their study of the Ta(s)/Cu(l) SLI, G.Q. Yang *et al.* [7] significant structural anisotropy was observed. The (111) interface was found to exhibit significant surface alloying at the interface, while the first Cu-layer at the Ta(100) interface was found to be crystalline, with a templated structure commensurate with the lattice structure of the underlying Ta substrate. The Ta(110)/Cu(l) SLI exhibited significant layering of the fluid at the surface, but with no surface alloying or templated structure.

In the present study, we employ classical and *ab initio* atomistic simulations to probe chemically heterogeneous Al(s)/Ga(l) SLIs. This system was chosen because of its major role in the study of liquid-metal embrittlement (LME). LME is a pathway of degradation common to polycrystalline metals having a high melting point (e.g., Al, certain steel alloys) in contact with liquid metals having a low melting point (e.g., Ga, Hg). In LME, the liquid metal penetrates into the grain boundaries between crystal domains, which reduces the strength and rigidity of the material. This embrittlement necessarily forms two SLIs in the place of a single grain-boundary interface. The newly formed interfaces are thermodynamically stable if $2\gamma_{sl} < \gamma_{gb}$, where γ_{sl} is the interfacial free energy of one of the (created) SLIs and γ_{gb} is that of the grain boundary. As a result of the widespread industrial use of aluminum, there is interest in developing a greater understanding of such polycrystalline aluminum under adverse conditions to improve the material and reduce degradation.

*blaird@ku.edu

The Al–Ga SLI stands out from other systems susceptible to LME in that the process does not require the application of tensile stress to occur [8–10]. This suggests that there is some characteristic specific to Al–Ga interfaces that drives LME to a greater extent than in other systems. The mechanism of Al–Ga LME has been studied using computational methods [11]; however, a general characterization of Al–Ga interfaces has not been carried out, experimentally or computationally. While there exist x-ray/TEM techniques for observing Al–Ga LME, the resolution is not sufficient to examine the interface confined between bulk solid and bulk liquid at the atomic level.

An isotropic embedded-atom method (EAM) potential for Al–Ga binary systems was developed by Nam *et al.* [12], who used the potential to simulate Ga penetration into the Σ5 symmetric tilt grain boundary of an Al bicrystal [11]. Despite the fact that their EAM model incorrectly predicts face-centered cubic (fcc) for the pure Ga ground-state crystal structure, the model gives a liquid structure and Al(s)/Gl(l) solid-liquid phase equilibrium consistent with experiment, although with a liquid density that is too high. Thus, it was considered in Ref. [12] to be an acceptable model for liquid Ga. However, it is an open question as to whether the model should be considered appropriate under the same conditions for a SLI, particularly if prefreezing or adsorption were to occur. This concern is especially relevant for Ga, as additional anisotropic terms are necessary to accurately reproduce the covalent dimer nature of Ga. We will use this model in our characterizations of planar interfacial Al–Ga systems, but, as a check on the final structures observed, supplement the classical simulations with *ab initio* molecular-dynamics (AIMD) calculations.

There are three distinct cases that have been observed for lateral structures of a liquid at a solid interface. (1) The intrinsic liquid structure persists up to the interface with little influence from the lateral structure of the substrate, as in the case of Pb–Si(100) [13]. (2) The liquid phase adopts a lateral structure resembling that of the stable crystalline phase of the liquid, as in the case for liquid Pb at Cu(111), as discussed above [3], or for Ga on diamond (111) [14]. (3) The solid substrate imposes a lateral symmetry on the liquid different than that of the liquid's intrinsic solid or liquid structure, as in the case of Bi on Cu(111) [15]. For Ga on diamond (111) at 300 K, a few (001) α-Ga planes of Ga_2 dimers are found between the hard diamond wall and the bulk supercooled Ga liquid. One possible explanation for this structure is that the introduction of a few crystalline dimeric layers of Ga decreases the abruptness of the transition from metallic bonding in liquid Ga to covalent bonding in diamond. [14] This suggests that Ga at a metallic interface should retain its metallic nature with covalent bonding suppressed.

The structure and transport kinetics of the planar Al–Ga interface is characterized in this study through the calculation of profiles for density, stress, potential energy, and diffusion as a function of the distance normal to the interface (here defined to be z). These quantities are calculated at 368 K for the three interfacial orientations (100), (110), and (111) to examine interfacial anisotropy. Note that, for this model, at this temperature an Al-rich crystalline solid (90.96% Al, 9.04% Ga) coexists with a Ga-rich liquid phase (98.6% Ga, 1.4% Al) [12]. (For simplicity, we will refer to the Al-rich crystal and Ga-rich liquid by their major components: Al or Ga, respectively.) To determine the structure parallel to the interfacial plane to atomic-level detail, we examine 2D density maps and Fourier transform structure factors. Interfacial excess energy and excess stress are calculated from the profiles.

II. COMPUTATIONAL DETAILS

For the classical molecular-dynamics (MD) simulations, we used the EAM many-body potential of Ref. [12] to model the Al-Ga system. The EAM potential of Nam *et al.* for the Al-Ga system [11,12] was designed to reproduce the experimental phase diagram and subsequently was used for the direct simulation of Ga penetration of Al grain boundaries [11,16]. To study liquid Ga at a solid Al surface, we chose to simulate the systems at 368 K, which corresponds to the first reported simulation data point on the EAM potential phase diagram calculated in Ref. [11], and represents a temperature of 63 K above the EAM fcc-Ga melting point, 305 K, as determined by MD phase coexistence calculations.

All classical MD simulations were performed using the LAMMPS MD code [17]. To enforce constant temperature and/or constant pressure, we used a Nosé-Hoover thermostat with a 0.1 ps relaxation time and/or an Anderson barostat with a 1.0 ps relaxation time, respectively [18]. A time step of 1 fs was used in all classical calculations. Periodic boundary conditions were applied for all three directions in all simulations, and the z axis represents the direction normal to the interfacial plane.

To construct the initial SLI configuration, we first created separate solid and liquid systems equilibrated at 368 K and 1 bar at compositions of mole fraction $x_{\mathrm{Ga}}^{\mathrm{sol}}(368\ \mathrm{K}) = 0.0904$ and mole fraction $x_{\mathrm{Ga}}^{\mathrm{liq}}(368\ \mathrm{K}) = 0.986$. These conditions represent those for the lowest temperature at which the phase equilibrium was determined computationally for this model in Ref. [11]. The crystal is equilibrated at constant isotropic pressure to ensure negligible excess stress. The corresponding liquid is separately equilibrated at constant cross-sectional area A_{xy} in an $NP_zA_{xy}T$ simulation.

The separate simulation boxes for the two phases are then placed in contact along the z axis with a separation of a few Å and allowed to come together at constant $P_z = 1$ bar, and an equilibrium combined system length L_z is found. Each simulation containing a SLI consisted of approximately 30 000 atoms. Finally, production data is collected in an NVT simulation at $V = A_{xy} \times L_z$. To avoid Brownian motion of the Al crystal slab, which can artificially broaden the calculated interfacial profiles, we subtract the linear momentum for the two innermost layers of the Al crystals during the NVT production simulations [19]. To improve the statistics, five independent 1-ns runs are chosen for these final NVT simulations for each crystal orientation. Because of periodic boundary conditions, each simulation box contains two interfaces, so we have ten independent interfaces from which to calculate interfacial properties. For reference, equilibrated snapshots from the classical MD simulations are shown in Fig. 1.

Although the current classical EAM potential for Al-Ga has been used with success in studying the Al-Ga interface, it is not without shortcomings (incorrect equilibrium Ga crystal and liquid densities), as discussed in the Introduction.

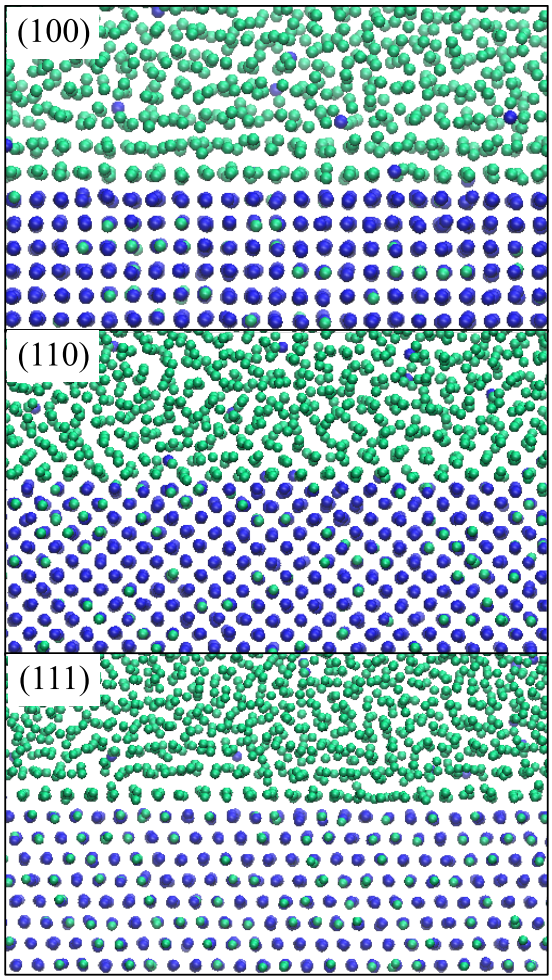

FIG. 1. Snapshots of the equilibrated Al–Ga (100), (110), and (111) interfaces at 368 K. Blue atoms represent Al, and green atoms represent Ga. All three interfaces are faceted.

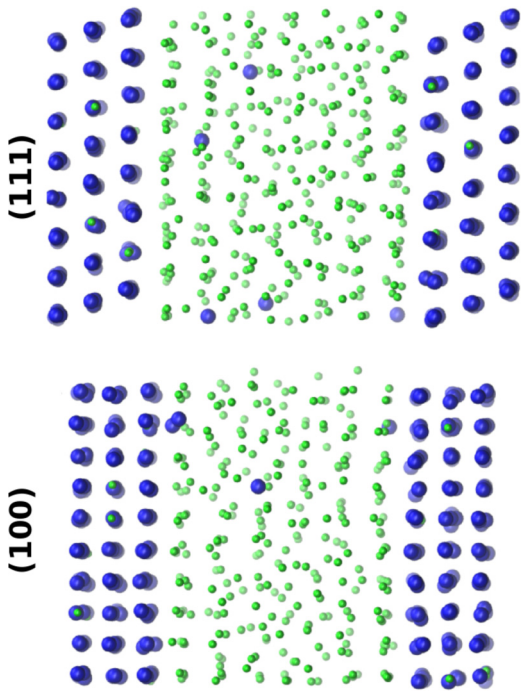

FIG. 2. Snapshots of the equilibrated Al(100)/Ga(l) and Al(111)/Ga(l) interfaces from the AIMD simulations at 368 K. Blue atoms represent Al, and green atoms represent Ga. Both interfaces are faceted.

Therefore, as a check, we have performed AIMD simulations to test whether templating of the first few layers of liquid onto the solid substrate is a robust finding or if it is an artifact of the potential. For these AIMD simulations, the aforementioned procedure was repeated to prepare a smaller scale version of the of the Al(100)/Ga and Al(111)/Ga SLIs, suitable for performing electronic structure calculations using the VIENNA AB INITIO SIMULATION PACKAGE (VASP) [20–22]. [The (110) SLI was not examined using AIMD because the lower density of the interfacial planes for this orientation made it difficult to get sufficient statistics in a reasonable amount of time.] The cross-section of the conjoined solid and liquid interface was approximately 20 Å per side. Each phase was prepared at the equilibrium experimental densities of 2.69 g/cm^3 for solid Al and 6.05 g/cm^3 for liquid Ga. The total number of atoms per simulation was 600 and 672 for Al(100)/Ga(l) and Al(111)/Ga(l), respectively. The solid and liquid phases were prepared at the equilibrium composition used in classical simulation compositions.

System energetics in the AIMD simulations were calculated within the generalized gradient approximation (PW91) [23,24] to the density-functional theory as implemented in VASP, employing the projector augmented wave function [25,26]. The choice of the generalized gradient approximation was made to ensure proper treatment of rapid changes in electron densities near the SLIs. All AIMD simulations were executed using a plane-wave basis set energy cutoff of 313.24 eV, a single k point (gamma centered) and time step of 3 fs within the NVT ensemble employing the Nosé-Hoover thermostat [27] at 368 K. A snapshot from the AIMD simulations for the Al(100)/Ga(l) and Al(111)/Ga(l) SLIs is shown in Fig. 2.

Because of the high computational expense of AIMD simulations, the systems studied were much smaller and simulated over shorter timescales than the MD simulations. To control for the effect of system size and equilibration time, we have also performed classical MD simulations of the same system size and run length as the AIMD runs.

A. Interfacial characterization

Interfacial profiles are used to characterize the change in system properties as the system is traversed along interface normal from bulk solid, though the interface and into the bulk liquid. Two types of profiles are calculated—fine scale and coarse grained. Fine scale profiles are determined by dividing the system into bins of width $\Delta z = 0.05$ Å along the z axis—defined as the axis perpendicular to the interfacial plane. The bin width Δz is chosen to be small relative to the interplanar spacing of the solid phase. For the system considered here, this value of Δz corresponds to approximately 41, 29, and 47 bins per lattice plane spacing for the (100), (110), and (111) orientations, respectively. Fine-scale profiles are calculated

for the density, potential energy, and excess stress. Diffusion constant profiles are also calculated, although on a coarser scale using bin widths that are larger than for the fine scale profiles of density, energy and stress.

For the density, potential energy, and stress profiles, we also calculate coarse-grained profiles by filtering and smoothing the fine-scale profiles using a finite-impulse-response (FIR) smoothing algorithm [19]. The various fine-scale interfacial profiles are calculated as follows:

(1) *Density profiles*: The density profiles for each species across the interface, $\rho_i(z)$, $i =$ Al or Ga, are computed as the average number of atoms in each discrete bin of width Δz divided by the volume of the bin, $V_z = A_{xy}\Delta z = L_x L_y \Delta z$,

$$\rho_i(z) = \frac{\langle N_i \rangle_z}{V_z}, \tag{1}$$

where $\langle N_i \rangle_z$ is the average number of atoms of type i in the bin.

(2) *Potential energy profiles*: The potential energy profile, $U(z)$, is computed by averaging the potential energy in discrete bins and dividing by the volume of the bins:

$$U(z) = \frac{\langle U \rangle_z}{V_z}. \tag{2}$$

(3) *Stress profiles*: The stress profile, $S(z)$, is determined as the difference between the normal and transverse components of the pressure tensor, averaged within the bin:

$$S(z) = P_{zz}(z) - \tfrac{1}{2}[P_{xx}(z) + P_{yy}(z)]. \tag{3}$$

(4) *Diffusion constant profiles*: To determine the diffusion constant profiles, we first assign the particles (at an initial time t_0) to coarse-grained bins in z, defined as the regions between the minima of the fine-grained density profiles. The diffusion constant in each bin is then determined from the slope of the average mean-square displacement as a function of time for the particles located in the bin at t_0,

$$D(z) = \lim_{t>t_D} \frac{1}{6}\frac{d}{dt}\langle [\mathbf{r}(t) - \mathbf{r}(t_0)]^2 \rangle_z, \tag{4}$$

where t_D is a time large enough that the dynamics is diffusive.

The FIR method is performed by taking a fine-scale profile f_n and applying the equation

$$\overline{f}_n = \sum_{k=-N}^{N} w_k f_{n+k} \tag{5}$$

to obtain the filtered components. The filter coefficients w_k have the form

$$w_k = A e^{-(k/\epsilon)^2}, \qquad k = -N, \ldots, N, \tag{6}$$

where ϵ is a parameter chosen to minimize the quantity

$$S = \sum_n (\overline{f}_{n-1} - 2\overline{f}_n + \overline{f}_{n+1})^2 \tag{7}$$

and A is a normalization constant determined by the constraint $\sum w_k = 1$. For the value of $N = 200$ used here, the resulting ϵ was generally in the range of 75 ± 10.

B. Interfacial lateral structure and symmetry

For each orientation, we also examine the 2D structure of the interfacial planes near the interface. Within these interfacial layers, we employ analysis on the average 2D density map, $\langle \rho_{xy}(\mathbf{r}) \rangle$, where the average includes all particles found within a specific interfacial plane, defined using a bin width equal to the trough-to-trough distance between minima in the density profile. The time-averaged 2D particle number density is calculated by averaging over 1000 configurations sampled over 1 ns. The underlying symmetries of the interfacial layers are examined by calculating the 2D structure factor $F_{xy}(\mathbf{k})$ [28],

$$F_{xy}(\mathbf{k}) = \langle |\rho_{xy}(\mathbf{k})|^2 \rangle, \tag{8}$$

in which $\rho_{xy}(\mathbf{k})$ is the Fourier transform of the 2D density function for each single configuration and the final average is taken over 1000 configurations. For the smaller scale AIMD simulations, averages are computed over a total simulation time of 50 ps involving 16 000 configurations. Additionally, the 2D structure factor was also calculated for two separate smaller scale classical simulations that were approximately the same size and of identical composition to that of the AIMD simulations. These two, separate, smaller scale classical simulations, also employing the EAM potential of Nam *et al.* [11,12] were averaged over 18 ns (200 configurations) and 50 ps (251 configurations), respectively.

C. Interfacial excess quantities

The calculation of interfacial excess quantities for a planar SLI requires the specification of a Gibbs dividing surface (GDS), which is a mathematical plane separating the solid and liquid phases. For a multicomponent system, the position of the GDS is commonly chosen such that the excess number of particles of one of the species is zero. As discussed before, the use of periodic boundary conditions generates two independent interfaces in the simulation box and, thus, two dividing surfaces are needed. Once the positions of these surfaces are specified, the interfacial excess for any extensive quantity Y is defined as

$$\begin{aligned} Y_{\text{ex}} &= \frac{1}{2A_{xy}}(Y - y_l V_l - y_s V_s) \\ &= \frac{1}{2}\left[\frac{Y}{A_{xy}} - y_l L_l - y_s L_s\right], \end{aligned} \tag{9}$$

where y_l and y_s are the bulk values of the quantity Y per unit volume in the liquid and solid, respectively, V_l, V_s, L_l and L_s are the volumes and $z-$direction lengths of the liquid and solid regions, as defined by the GDS. The factor of 2 arises because there are two independent interfaces in each simulation box. In terms of total box length ($L_z = L_l + L_s$), we have

$$y_{\text{ex}} = \frac{1}{2}\left[\frac{Y}{A_{xy}} - y_l L_z - (y_s - y_l)L_s\right]. \tag{10}$$

In this paper, we chose a dividing surface in which the excess number of Al atoms is equal to zero,

$$\Gamma_{\text{Al}} = \frac{1}{2}\left[\frac{N_{\text{Al}}}{A_{xy}} - \rho^l_{\text{Al}} L_z - (\rho^s_{\text{Al}} - \rho^l_{\text{Al}})L_s\right] = 0, \tag{11}$$

where N_{Al} is the total number of particles of Al and ρ^l_{Al} and ρ^s_{Al} are the densities of Al in the liquid and solid, respectively. The position of the dividing surface is then determined by solving for the length of the solid:

$$L_s = \left[\frac{N_{\mathrm{Al}}}{A_{xy}} - \rho^l_{\mathrm{Al}} L_z\right](\rho^s_{\mathrm{Al}} - \rho^l_{\mathrm{Al}})^{-1}. \tag{12}$$

In this study, we focus on three interfacial excess quantities: excess interfacial energy, $e^{(\mathrm{Al})}$, excess interfacial stress, τ, and excess interfacial number of Ga atoms, $\Gamma^{(\mathrm{Al})}_{\mathrm{Ga}}$, where the superscript (Al) denotes that these quantities were calculated using a dividing surface defined such that the excess number of Al atoms is zero. The values of $e^{(\mathrm{Al})}$ and $\Gamma^{(\mathrm{Al})}_{\mathrm{Ga}}$ are calculated according to Eq. (10), with Y being the total potential energy or number of Ga atoms, respectively. The interfacial excess stress τ is calculated directly in the MD simulation from the difference between the normal and transverse components of the overall average pressure tensor [19,29]:

$$\tau = P_{zz} - \left(\frac{P_{xx} + P_{yy}}{2}\right). \tag{13}$$

In general, the values of interfacial excess quantities will depend upon the definition of GDS used; however, for a planar interface, the value will be independent of GDS if the bulk limiting value of the quantity is the same in the solid and liquid. This is true for the stress, which is zero in equilibrium for both bulk phases, but not for the excess energy or excess particle number. Therefore, both the excess interfacial energy and particle number will depend upon the GDS definition, but not the excess interfacial stress.

III. RESULTS AND DISCUSSION

A. Perpendicular and lateral structure

The fine-scale density profiles, $\rho_{\mathrm{Al}}(z)$ and $\rho_{\mathrm{Ga}}(z)$, are shown in Fig. 3 for the (100), (110), and (111) Al-Ga interfaces. In all profiles shown, the position $z = 0$ corresponds to the GDS ($\Gamma_{\mathrm{Al}} = 0$), i.e., $z < 0$ for the solid and $z > 0$ for the liquid. For use in the subsequent analysis, selected peaks are labeled in Fig. 3 as S1 (first solid peak), L1–L3 (first through third liquid peaks).

In the solid region, the profiles show peaks corresponding to the Al-Ga alloy crystal planes, with spacing and widths corresponding to the geometry of the specific interfacial orientation. As the interface is approached from the solid, the solid density peaks decrease in amplitude (and increase in width), corresponding to an increase in the Debye-Waller factors of the crystal as the interface is approached. All interfaces are faceted, with well-separated solid and liquid density curves.

The density profiles in the liquid phase show significant structural ordering normal to the interfacial plane, which decays to the bulk values after about 8–15 Å from the GDS, depending upon the specific interfacial orientation. Such structural ordering is typical for liquids at a solid surface. Typically, for chemically heterogeneous SLIs, the spacing between the liquid peaks is controlled by the length scale defined by the first peak in the liquid structure factor and is independent of the crystal orientation. In the present case,

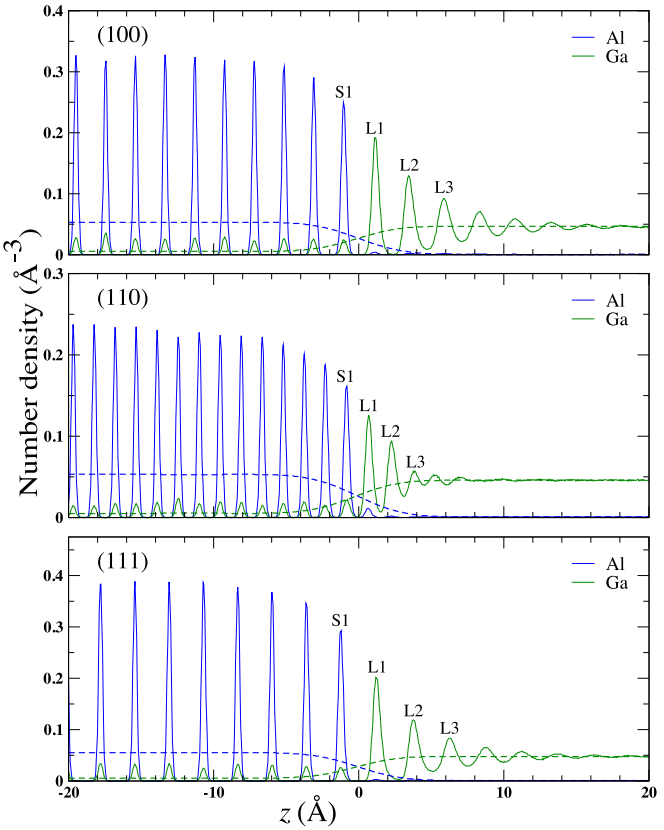

FIG. 3. Average density profiles for the Al–Ga solid–liquid interface (as determined by Eq. 1) for the (100), (110), and (111) interfacial orientations. The dashed lines represent smoothed (coarse-grained) density profiles obtained with the FIR method. The GDS is located at $z = 0$ in each plot. The labels S1 and L1–L3 are as defined in the text.

however, the liquid peaks nearest to the interface are spaced similarly to the crystal spacing in the corresponding solid. In the analysis to follow, we will show that this is due to the commensurate adsorption of the first few layers of the liquid phase onto the solid-substrate lattice. This behavior is also seen in the corresponding Al and Ga density profiles for the AIMD simulations for the (100) and (111) interfaces, shown in Fig. 4. To test the effect of the short timescales over which the AIMD simulations are run, we compare in Fig. 5 the AIMD *total* number density profiles with those from two additional classical MD simulations of the same system size used in the AIMD simulations. In the first, the classical system is advanced for the same duration as for the AIMD simulations—77 and 121 ps for (111) and (100), respectively. In the second classical run, both orientations are run for a full 20 ns. Figure 5 shows that the density profiles of the classical simulations have converged on the timescale of the AIMD runs, indicating that, even though the AIMD simulations are of short duration, they are sufficiently long for the system to reach structural equilibrium. For the (100) interface, the AIMD and classical MD density profiles are in near quantitative agreement. Similar results are seen for (111), except for a small difference in liquid peak spacing between the AIMD and classical MD simulations.

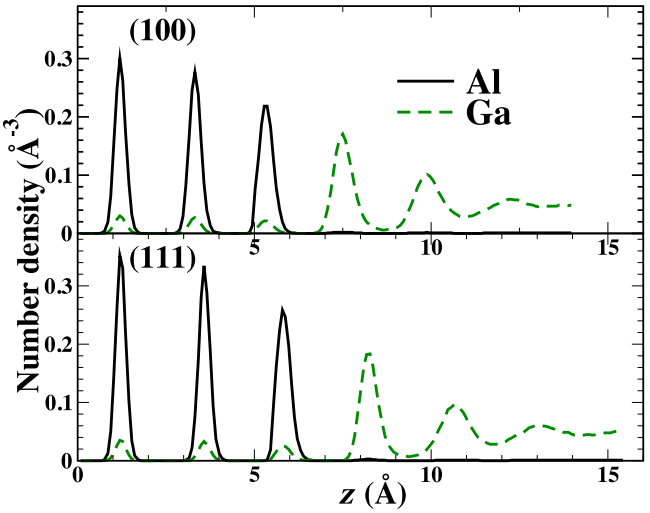

FIG. 4. Al and Ga number density profiles for the Al(111)/Ga(l) (top panel) and Al(100)/Ga(l) (bottom panel) SLIs from AIMD simulations.

To further understand the structure at the interface, Fourier analysis is used to calculate the 2D structure factors for the interfacial planes surrounding the interface for each interfacial orientation studied in the classical MD simulations. The results are shown in Fig. 6, where the labels S1 and L1-L3 correspond to the first solid and first three liquid interfacial planes, respectively (see Fig. 3). These 2D structure factors give a more detailed picture of the in-plane ordering. For the plane S1, the structure factors show Bragg peaks consistent with the corresponding crystal planes of the solid substrate. For all orientations studied, the first plane on the liquid Ga side of the interface (L1) shows an in-plane structure that is commensurate with the underlying crystal lattice, indicating that the first layer of the Ga liquid occupies positions that represent a continuation of the substrate lattice. The lattice constant for these adsorbed layers is the same as that of the Al-Ga crystalline substrate—4.10 Å versus 4.25 Å for fcc Ga. Therefore, this is not simply a case of "prefreezing" of the Ga liquid at the surface, but represents an epitaxial adsorption of the first one to two layers of Ga onto the substrate surface structure. The extent to which this templating extends into the liquid phase depends upon the interfacial orientation—for (111), only the first liquid layer is affected significantly, whereas for (100), and especially for (110), this in-plane ordering extends (weakly) into the third layer of liquid Ga.

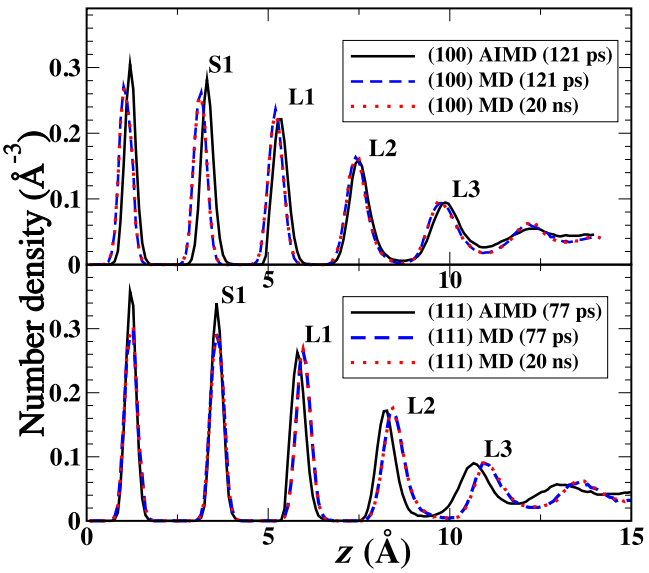

FIG. 5. Comparison of the *total* density profiles for the Al(100)/Ga(l) (top panel) and Al(100)/Ga(l) (bottom panel) SLIs from the AIMD simulations and two classical MD simulations—one using the same equilibration times as the AIMD simulations [77 and 121 ps for (111) and (100), respectively] and, for comparison, one for a much longer run (20 ns).

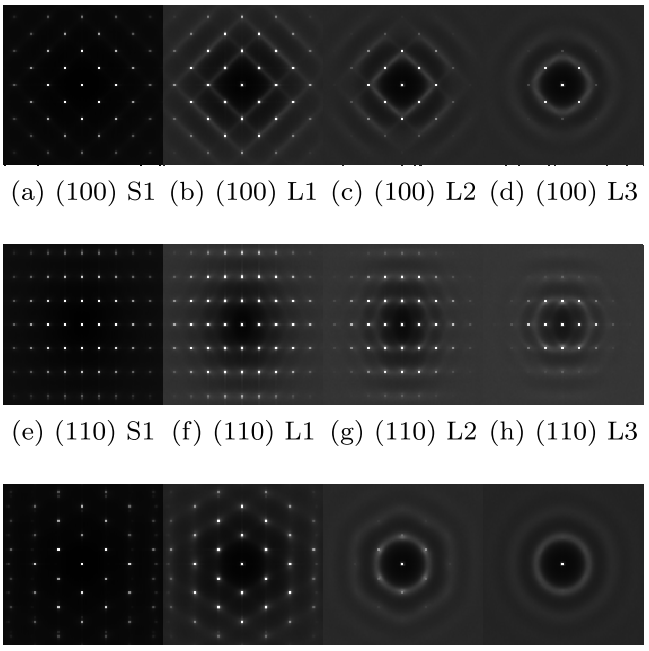

FIG. 6. Average 2D structure factors from the classical MD simulations for the (100) [top, (a)–(d)], (110) [middle, (e)–(h)], and (111) [bottom, (i)–(l)] orientations, as determined using Eq. (8). The labels S1 and L1–L3 correspond to the last solid and first three liquid layers as defined by the GDS and as labeled in Fig. 3.

The 2D structure factor results from the AIMD simulations are shown in the top panels of Figs. 7(a)–7(d) and 8(a)–8(d) for the Al(100)/Ga(l) and Al(111)/Ga(l) interfaces, respectively. For these AIMD simulations, the first Ga layer in the (b) panels shows a crystalline symmetry commensurate with the Al surface orientation and lattice spacing—in agreement with the classical results. The second Ga layer also shows some ordering, but to a much diminished extent. We have also computed the 2D structure factors for the two smaller classical MD simulations discussed in the previous subsection. The structure factor for the shorter duration classical simulations are shown in Figs. 7(e)–7(h) and 8(e)–8(h) and those for the longer (20 ns) classical simulations are shown in Figs. 7(i)–7(l) and 8(i)–8(l). Figures 7(e)–7(h) and 8(e)–8(h) show the 2D structure factors for similarly smaller scale classical simulations of comparable total simulation times (i.e., 50 ps)

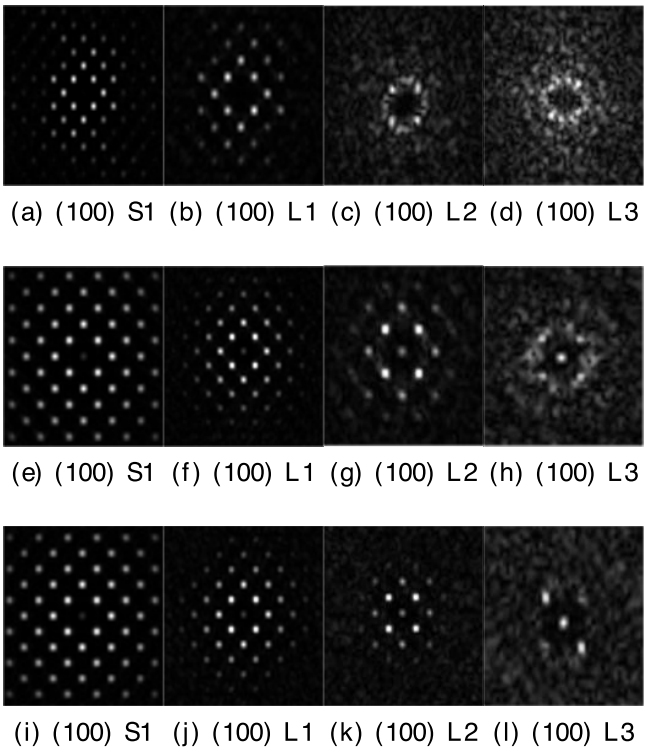

FIG. 7. Average 2D structure factors for Al(100)/Ga interfacial planes: (a)–(d), top, AIMD simulations (50 ps averages); (e)–(h), middle, classical MD simulations (50 ps averages, small size); (i)–(l), bottom, classical MD simulations (20 ns averages, small size). Four structure factors are given, from left to right, for layers corresponding to the first interfacial solid peak and the first, second, and third liquid peaks from the density profile, as denoted in Fig. 3.

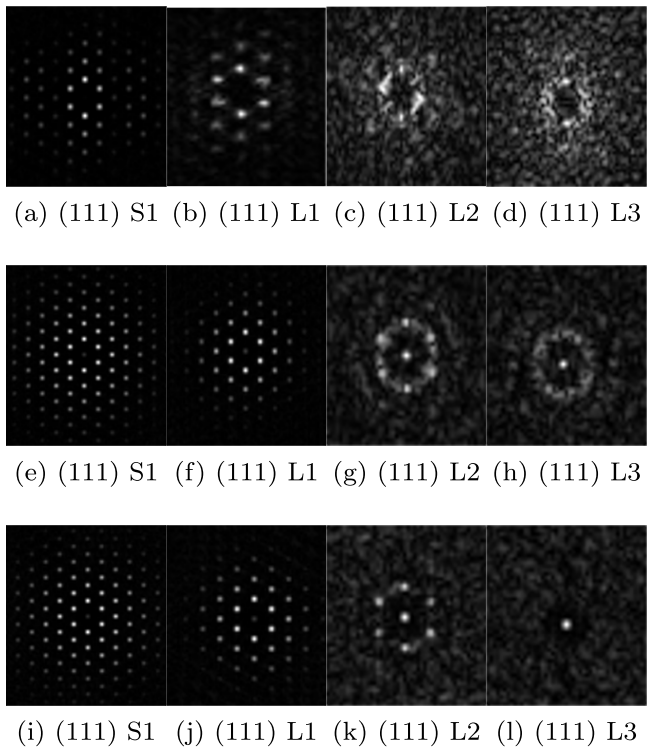

FIG. 8. Average 2D structure factors for Al(111)/Ga interfacial planes: [(a)–(d), top] AIMD simulations (50 ps averages); (e)–(h), middle, classical MD simulations (50 ps averages, small size); (i)–(l), bottom, classical MD simulations (20 ns averages, small size). Four structure factors are given, from left to right, for layers corresponding to the first interfacial solid peak and the first, second, and third liquid peaks from the density profile, as denoted in Fig. 3.

to that of the AIMD simulations. Even at a comparable total simulation time of 50 ps, the smaller scale classical simulations, for both Al facets, show a higher degree of liquid ordering (i.e., two layers of Ga liquid ordering as opposed to one for the AIMD simulations). Additionally, Figs. 7(a)–7(d) and 8(a)–8(d) also depict 2D structure factor results of similarly smaller scale classical simulations albeit with a total run time of 20 ns. These latter results are also consistent with those for the larger scale systems (see Fig. 6). Thus, for the simulation size scales (square interfacial plane with side length of 20 Å up to 80 Å) probed in this study and for simulation times as short as 50 ps, epitaxial Ga adsorption commensurate with the lattice spacing of the Al(100) or Al(111) solid surfaces is quickly induced upon contact. The AIMD simulations show that the observations of epitaxial ordering of Ga at the SLI in the classical simulations are robust, albeit significantly weaker beyond the first Ga layer.

B. Interfacial profiles and excess values of energy, stress, and composition

The smoothed interfacial energy and stress profiles for the (100), (110), and (111) interfacial orientations at 368 K are plotted in Figs. 9 and 10. The stress profiles in Fig. 10 show approximately zero stress in both the bulk liquid and the bulk solid. For a solid–liquid interface under hydrostatic stress, $S(z)$ measures the difference between the longitudinal and transverse average pressures, and zero stress in the bulk regions indicates that all interfaces have been properly equilibrated under hydrostatic conditions.

The different orientations have different stress profiles. While the (110) and (111) interfaces exhibit only a strong negative peak, the (100) shows a small positive peak on the side of the solid and a modest negative peak on the side of the liquid. In contrast, the potential energy profiles in Fig. 9 show little anisotropy.

Interfacial excess values are tabulated in Table I. For all orientations, the excess number of gallium atoms at the interface is positive. As a result, the total stress for all of the

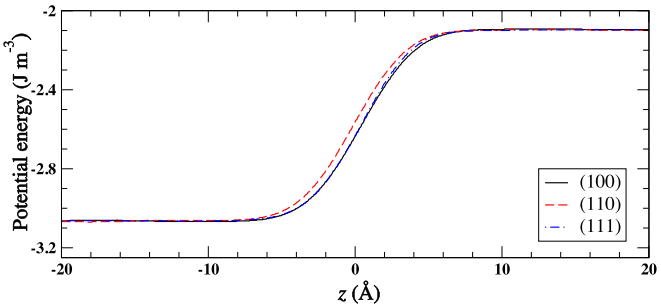

FIG. 9. Average potential energy profiles for the three interfacial orientations as determined by Eq. (2).

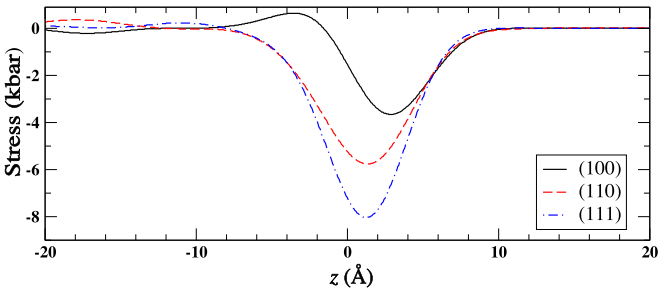

FIG. 10. Average stress profiles for the three interfacial orientations as determined by Eq. (3). While the (110) and (111) orientations show a large negative peak (corresponding to compressive stress), the (100) orientation shows a small positive peak on the side of the solid and a moderate negative peak on the side of the liquid.

orientations is negative, which can be attributed to the modest to strong negative peaks in the stress profiles on the Ga-rich liquid side of the interfaces. Using the Gibbs-Cahn equation [30–32],

$$\frac{1}{A}\frac{d(\gamma A/T)}{dT} = -\frac{e}{T^2} + \frac{\tau}{AT}\frac{dA}{dT}, \tag{14}$$

the excess stress, τ, and excess energy, e, can be used to calculate changes in the interfacial free energy, γ.

C. Diffusion constant profiles

The average diffusion coefficients for the first seven liquid layers are shown in Figs. 11–13. Both the individual components of D (in the x, y and z directions) and the orientationally averaged value are calculated. For the calculation of diffusion coefficients, additional simulations were performed so that atomic positions could be output more frequently, every 100 fs. Averages for each layer are taken over ten independent simulations of 10 ps each, with 20 independent diffusion coefficients determined for each point from fitting mean-square displacements in the range 1–10 ps. For the first liquid peak (L1) for each orientation, the diffusion coefficient is very nearly zero, consistent with the epitaxial adsorption of this layer to the substrate. For the subsequent layers, the diffusion constants increase monotonically until the bulk value of about 2.7×10^{-9} m^2/s is reached about a distance of 15 Å away from the GDS. The diffusion coefficients show significant anisotropy even as far out as 8–10 Å from the GDS, indicating that the lateral structure of the substrate is influencing the liquid dynamic several layers into the liquid phase.

TABLE I. Al–Ga interfacial parameters at 368 K. Determined from the FIR smoothed density profiles and equations. All parameters are averaged over 5 ns simulations treated as five statistically independent blocks.

	τ (J m^{-2})	$e^{(\mathrm{Al})}$(J m^{-2})	$\Gamma_{\mathrm{Ga}}^{(\mathrm{Al})}$ (Å^{-2})
(100)	–0.172(9)	–0.70(5)	0.0121(12)
(110)	–0.433(4)	–1.37(3)	0.0288(2)
(111)	–0.511(9)	–0.75(3)	0.0082(3)

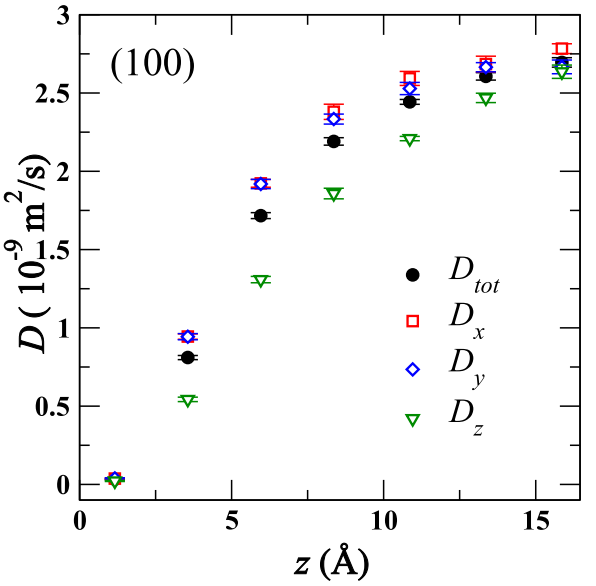

FIG. 11. Average diffusion coefficients for the (100) interfacial orientation as a function of distance from the GDS as determined by Eq. (4).

IV. CONCLUSION

Using an EAM potential and MD simulation, we have examined the chemically heterogeneous interface between solid Al and liquid Ga at 368 K. To determine the anisotropy of the properties of this interface, three different orientations were studied: (100), (110), and (111). For each of these orientations, the structure of the interface was characterized through the calculations of density profiles, as a function of distance along the interface normal, as well as 2D Fourier analysis of the lateral interfacial planes within the interfacial region. Interfacial thermodynamics was studied through

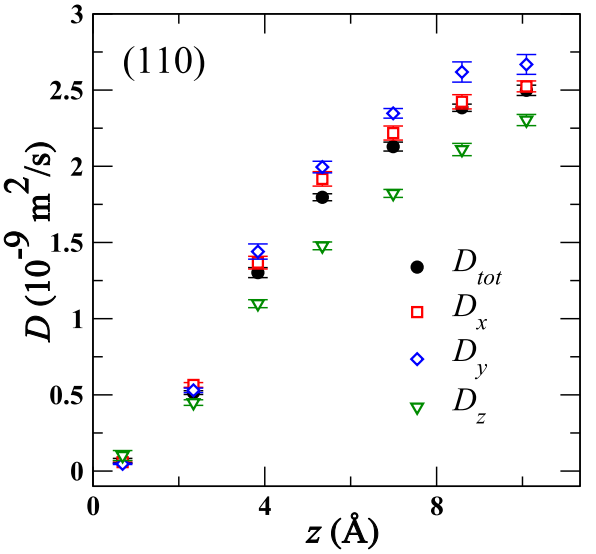

FIG. 12. Average diffusion coefficients for the (110) interfacial orientation as a function of distance from the GDS as determined by Eq. (4).

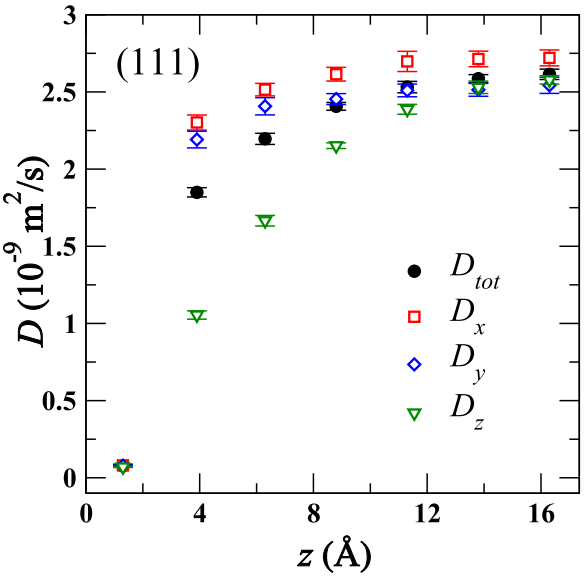

FIG. 13. Average diffusion coefficients for the (111) interfacial orientation as a function of distance from the GDS as determined by Eq. (4).

interfacial profiles of energy and stress, and diffusion constant profiles were determined to examine the dependence of transport properties on position relative to the interfacial dividing surface.

The epitaxial adsorption of Ga at the Al surface seen here is similar to that seen in simulations of the Ta(100)/Cu(l) SLI [7] but qualitatively different from that seen in the other Ta(s)/Cu(l) orientations and in other recently studied chemically heterogeneous metal-metal SLIs, such as Cu(s)/Pb(l) and Al(s)/Pb(l) SLIs. In the present Al(s)/Ga(l), the first layer of Ga is observed to epitaxially adsorb to the Al surface with a lattice spacing commensurate with the Al substrate. In contrast to the Ta(100)/Cu(l) SLI [7], this epitaxial adsorption is present independent of Al surface orientation. This results in significant compressive stress at the interface, and demonstrates that the stress observed in the direct simulation of Al–Ga LME [11] is not specific to the bicrystal system studied therein. The epitaxial ordering of the first layer of Ga on the Al substrate is also observed in smaller-scale AIMD simulations, albeit with somewhat weaker ordering than is observed in the classical simulations, especially beyond the first layer. However, the AIMD simulations show that, at least qualitatively, the epitaxial ordering seen here is not merely an artifact of the EAM potential used. Characterization of diffusion near the interfacial region shows that the dynamics of liquid Ga is affected by the structure of the substrate even several layers distant from the interface.

ACKNOWLEDGMENTS

We gratefully acknowledge support for this work from the National Science Foundation (NSF) under Grant No. CHE-1465226. We also wish to thank Prof. Mark Asta for helpful discussions.

[1] W. Kaplan and Y. Kauffman, Annu. Rev. Mater. Res. **36**, 1 (2006).
[2] P. Geysermans, D. Gorse, and V. Pontikis, J. Chem. Phys. **113**, 6382 (2000).
[3] J. P. Palafox-Hernandez, B. B. Laird, and M. Asta, Acta Mater. **59**, 3137 (2011).
[4] J. P. Palafox-Hernandez and B. B. Laird, J. Chem. Phys. **145**, 211914 (2016).
[5] Y. Yang, D. Olmsted, M. Asta, and B. B. Laird, Acta Mater. **60**, 4960 (2012).
[6] Y. Yang, M. Asta, and B.B. Laird, Phys. Rev. Lett. **110**, 096102 (2013).
[7] G. Yang, J. Li, Q. Shi, and L. Kong, Comp. Mater. Sci **86**, 64 (2014).
[8] H. K. Huntington, J. Inst. Metals **11**, 108 (1973).
[9] W. Ludwig, D. Bellet, J. Teyssier, J. Ouillier, N. Marie, K. Wolski, A. Simionovici, and C. Rau, J. Phys. IV France **12**, 289 (2002).
[10] W. Ludwig, E. Pereiro-López, and D. Bellet, Acta Mater. **53**, 151 (2005).
[11] H.-S. Nam and D.J. Srolovitz, Phys. Rev. B **76**, 184114 (2007).
[12] H.-S. Nam, M.I. Mendelev, and D. J. Srolovitz, Phys. Rev. B **75**, 014204 (2007).
[13] H. Reichert, O. Klein, H. Dosch, M. Denk, V. Honkimäki, and T. Lippmann, Nature **408**, 839 (2000).
[14] W. Huisman, J. Peters, M. Zwanenburg, S. de Vries, T. Derry, D. Abernathy, and J. van der Veen, Nature **390**, 379 (1997).
[15] D. Kaminski, P. Poodt, E. Aret, N. Radenovic, and E. Vlieg, Phys. Rev. Lett. **96**, 056102 (2006).
[16] H.-S. Nam and D.J. Srolovitz, Phys. Rev. Lett. **99**, 025501 (2007).
[17] S. Plimpton, J. Comput. Phys. **117**, 1 (1995).
[18] D. Frenkel and B. Smit, *Understanding Molecular Simulation*, 2nd ed. (Academic Press, New York, 2002).
[19] R. Davidchack and B. Laird, J. Chem. Phys. **108**, 9452 (1998).
[20] G. Kresse and J. Hafner, Phys. Rev. B **47**, 558 (1993).
[21] G. Kresse and J. Hafner, Phys. Rev. B **49**, 14251 (1994).
[22] G. Kresse and J. Furthmuller, Phys. Rev. B **54**, 11169 (1996).
[23] J.P. Perdew and Y. Wang, Phys. Rev. B **45**, 13244 (1992).
[24] J.P. Perdew, K. Burke, and M. Ernzerhof, Phys. Rev. Lett. **77**, 3865 (1996).
[25] P. E. Blochl, Phys. Rev. B **50**, 17953 (1994).
[26] G. Kresse and D. Joubert, Phys. Rev. B **59**, 1758 (1999).
[27] W.G. Hoover, Phys. Rev. A **31**, 1695 (1985).
[28] N. W. Ashcroft and D. N. Mermin, *Solid State Physics* (Thomson Learning, Toronto, 1976).
[29] S. W. Sides, G. S. Grest, and Martin-D. Lacasse, Phys. Rev. E **60**, 6708 (1999).
[30] B.B. Laird, R. Davidchack, Y. Yang, and M. Asta, J. Chem. Phys. **131**, 114110 (2009).
[31] T. Frolov and Y. Mishin, Phys. Rev. B **79**, 045430 (2009).
[32] T. Frolov and Y. Mishin, J. Chem. Phys **131**, 054702 (2009).